

9-1981

Elastic Wave Scattering from Multiple and Odd Shaped Flaws

Vasundara V. Varadan
Ohio State University

Vijay K. Varadan
Ohio State University

D. J. N. Wall
Ohio State University

Follow this and additional works at: http://lib.dr.iastate.edu/cnde_yellowjackets_1981

 Part of the [Materials Science and Engineering Commons](#)

Recommended Citation

Varadan, Vasundara V.; Varadan, Vijay K.; and Wall, D. J. N., "Elastic Wave Scattering from Multiple and Odd Shaped Flaws" (1981). *Proceedings of the DARPA/AFWAL Review of Progress in Quantitative NDE, October 1979–January 1981*. 45.
http://lib.dr.iastate.edu/cnde_yellowjackets_1981/45

This 10. Ultrasonic Scattering from Irregular Flaws is brought to you for free and open access by the Interdisciplinary Program for Quantitative Flaw Definition Annual Reports at Iowa State University Digital Repository. It has been accepted for inclusion in Proceedings of the DARPA/AFWAL Review of Progress in Quantitative NDE, October 1979–January 1981 by an authorized administrator of Iowa State University Digital Repository. For more information, please contact digirep@iastate.edu.

Elastic Wave Scattering from Multiple and Odd Shaped Flaws

Abstract

Using the T-Matrix or Null Field method elastic wave scattering from the following geometries have been studied (a) Rotationally symmetric configurations consisting of two spheroidal cavities separated by a finite distance and with different eccentricities. Exact calculations are compared with single scattering approximations. The frequency spectra are interpreted for various scattering geometries and compared with experiments. The effect of change in distance between the scatterers is also discussed. (b) Scattering from rotationally symmetric cavities with odd shapes like "Pinnochio", Rockwell Science Center sample #73 and "Micky Mouse", Rockwell Science Center sample #70 was also studied and compared with numerical results using other techniques as well as experiments. Several ways of studying such problems is also discussed. (c) A numerical technique is proposed to study dynamic stress concentrations.

Keywords

Nondestructive Evaluation

Disciplines

Materials Science and Engineering

V. V. Varadan, V. K. Varadan and D. J. N. Wall
Wave Propagation Group
Department of Engineering Mechanics
The Ohio State University
Columbus, Ohio 43210

ABSTRACT

Using the T-Matrix or Null Field method elastic wave scattering from the following geometries have been studied (a) Rotationally symmetric configurations consisting of two spheroidal cavities separated by a finite distance and with different eccentricities. Exact calculations are compared with single scattering approximations. The frequency spectra are interpreted for various scattering geometries and compared with experiments. The effect of change in distance between the scatterers is also discussed. (b) Scattering from rotationally symmetric cavities with odd shapes like "Pinocchio", Rockwell Science Center sample #73 and "Micky Mouse", Rockwell Science Center sample #70 was also studied and compared with numerical results using other techniques as well as experiments. Several ways of studying such problems is also discussed. (c) A numerical technique is proposed to study dynamic stress concentrations.

INTRODUCTION

The study of elastic wave scattering from two cavities has important implications from an NDE and fracture mechanics point of view. In many practical applications it is desirable to find out whether the flaw is a single one or two closely spaced ones separated by a small distance. In the latter case, it may be quite likely that the two flaws (cracks) will propagate towards each other according to fracture mechanics principles increasing the possibility of failure. In such cases, dynamic stress concentrations on the surface of each cavity particularly at corners and edges becomes relevant. This report deals with the scattering from two flaws separated by a finite distance (Fig. 1), odd shaped or compound flaws (Fig. 2) and the study of dynamic stress concentrations on the boundary of infinitely long cylindrical samples (2-D problems) with singular corners (Fig. 3). Whenever possible theoretical results are compared with available experimental results.

In a previous report¹, we gave a self-consistent formulation to obtain the T-matrix of two flaws separated by a finite distance. The expression that we obtained was identical to that given earlier by Peterson and Ström² for electromagnetic wave scattering from a configuration of two scatterers. Recently Boström³ has obtained limited numerical results for elastic wave scattering from two cavities. Using the expression for the T-matrix as given in Ref. 1, we have made calculations of the scattering from dissimilar or similar spheroidal cavities for a range of frequencies and a variety of scattering geometries. In all these calculations the configuration is rotationally symmetric about the chosen z-axis. We also give a T-matrix formulation for configurations without rotational symmetry in a subsequent section. This study is still in progress. Numerical results for rotationally symmetric configurations are discussed from an NDE point of view.

Following the discussion of two scatterers, the problem of elastic wave scattering from a compound flaw is presented. As the name suggests, this problem can be viewed as the scattering from a single odd shaped flaw or as a multiple scattering

problem of two flaws that are touching each other. Both methods are discussed.

Lastly for a two dimensional example of SH-wave incidence on a cylinder whose cross-section has sharp corners, the dynamic stress concentration around the boundary is studied for several frequencies and angles of incidence. Details of this calculation may be found in a separate report by Wall, Varadan and Varadan⁴.

DISCUSSION OF RESULTS FOR ROTATIONALLY SYMMETRIC CONFIGURATIONS OF TWO SCATTERERS

Plane harmonic elastic waves are incident on the configuration shown in Fig. 1. Both flaws that are separated by a distance '2d' are figures of revolution about the common z-axis. Thus, without loss of generality the plane of incidence can be assumed to be the x-z plane. Let \vec{u}^0 and \vec{u}^s be the displacement fields due to the incident and scattered waves, given by

$$\vec{u}^0 = \hat{p} e^{i\vec{k} \cdot \vec{r}} = \sum_{\tau=1}^3 \sum_{n m \sigma} a_{\tau n m \sigma}(\hat{p}, \hat{k}) \text{Re } \vec{\psi}_{\tau n m \sigma}(k\vec{r}) \quad (1)$$

where \hat{p} is the polarization vector, $\hat{k} = \vec{k}/|\vec{k}|$ defines the direction of propagation of the incident wave and $|\vec{k}| = \omega/c$, where 'c' is either the velocity of P- (longitudinal) waves or S- (transverse) waves depending on \hat{p} . The vector $\text{Re } \vec{\psi}$ is the vector spherical function that is regular at the origin. Explicit expressions for these and the associated normalization factors may be found in Ref. 5. The scattered field \vec{u}^s may be represented as

$$\vec{u}^s(\vec{r}) = \sum_{\tau=1}^3 \sum_{n m \sigma} f_{\tau n m \sigma} \vec{\psi}_{\tau n m \sigma}(k\vec{r}). \quad (2)$$

The expansion coefficients f are unknown and the function $\vec{\psi}$ is the vector spherical function that is outgoing at infinity (see Ref. 5). Our aim is to relate the unknown 'f' to the known 'a' via the T-matrix of the configuration.

In Ref. 1 an expression was obtained for the T-matrix by considering the total field incident on each scatterer and generalizing the definition of the T-matrix. Translation theorems for the spherical basis functions had to be invoked to have a common origin for the coordinate system for the two flaws. The final expression that was obtained can be cast into the form

$$T(1,2) = R(\vec{d})T^1 \{I - \sigma(-2\vec{d})T^2\sigma(2\vec{d})T^1\}^{-1} \times \\ \{I + \sigma(-2\vec{d})T^2R(2\vec{d})R(-\vec{d}) \\ + R(-\vec{d})T^2\{I - \sigma(2\vec{d})T^1\sigma(-2\vec{d})T^2\}^{-1} \\ \{I + \sigma(2\vec{d})T^1R(-2\vec{d})R(\vec{d})\} \quad (3)$$

where $2\vec{d}$ is the vector joining the centers O_1 and O_2 of the two obstacles, T^1 and T^2 are the T-matrices of the individual systems with respect to parallel coordinate systems centered at O_1 and O_2 respectively and $T(1,2)$ is the T-matrix of the configuration. Details of calculating T^1 and T^2 may be found in Ref. 5. The matrices R and σ are translation matrices, convenient expressions for which are given in Ref. 3.

The scattered field coefficients may now be written in vector matrix notation as

$$f = T(1,2)a. \quad (4)$$

For incident P-waves, the coefficients 'a' of Eq. (1) are given as

$$a_{\tau n m \sigma} = 4\pi \sqrt{\frac{c_p}{c_s}} \epsilon_{nm} i^{n-1} p_n^m(\cos \alpha) \begin{cases} \cos m\beta; \sigma = 1 \\ \sin m\beta; \sigma = 2 \end{cases} \quad (5) \\ \epsilon_{nm} = \sqrt{\frac{\epsilon_m (2n+1)(n-m)!}{4\pi(n+m)!}}$$

where (α, β) define the vector k . In all numerical calculations, $\beta = 0$, since the x-z plane is taken as the plane of incidence.

As the distance $2\vec{d}$ between the scatterers becomes large, the expression for $T(1,2)$ as given in Eq. (3) is unsuitable for numerical computations since the matrix elements of $R(2\vec{d})$ become rather large. In this case it is more convenient to use certain analytic properties of the R-matrix when it operates on the plane wave associated with the incident field and the outgoing spherical wave associated with the scattered field at distances far from the scatterer. This was first suggested by Peterson and Ström². Using this idea, the T-matrix simplifies to the following form

$$T(1,2) \xrightarrow{|\vec{r}| \rightarrow \infty} \exp i(k_p d \cos \alpha - k_\tau d \cos \theta) \times \\ T^1 \{I - \sigma(-2\vec{d})T^2\sigma(2\vec{d})T^1\}^{-1} \times \\ \{I + \sigma(-2\vec{d})T^2 \exp(2ik_p d \cos \alpha)\} \\ + \exp i(k_\tau d \cos \theta - k_p d \cos \alpha) \times \\ T^2 \{I - \sigma(2\vec{d})T^1\sigma(-2\vec{d})T^2\}^{-1} \times \\ \{I + \sigma(2\vec{d})T^1 \exp(-2ik_p d \cos \alpha)\}. \quad (6)$$

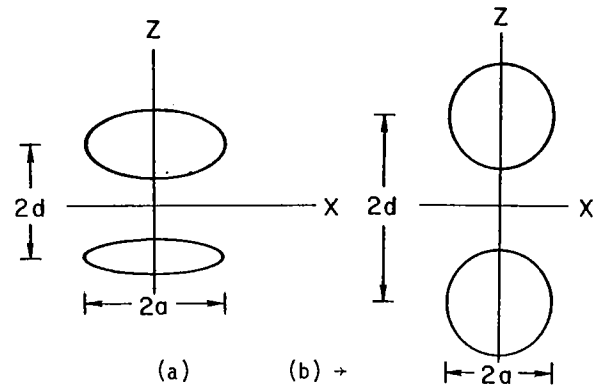


Fig. 1 Rotationally symmetric two scatterer configurations (a) Dissimilar spheroids (b) Identical spheres (c) Dissimilar spheres.

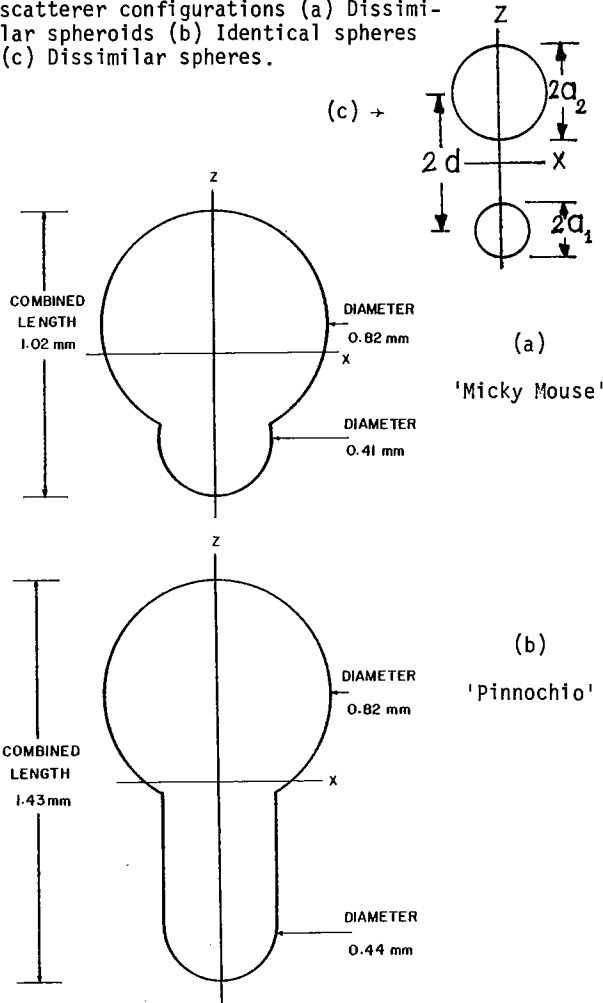


Fig. 2 Rotationally symmetric compound flaws.

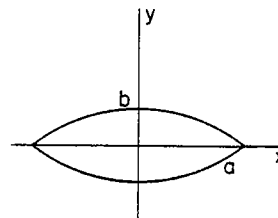


Fig. 3 Cylindrical cavity with sharp corners.

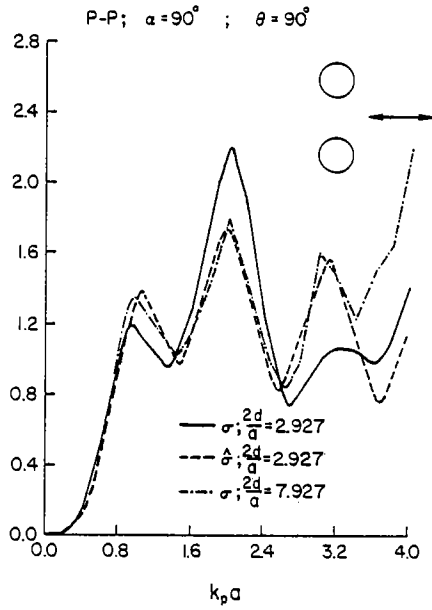


Fig. 4 Back scattering cross section as a function of frequency of identical spheres for incident P-waves.

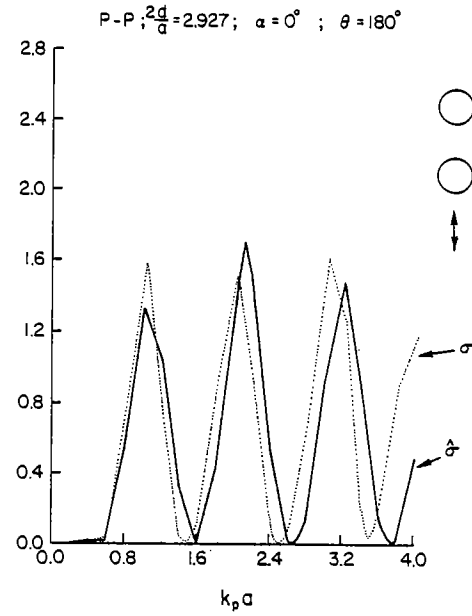


Fig. 5 Back scattering cross section as a function of frequency of identical spheres for incident P-waves.

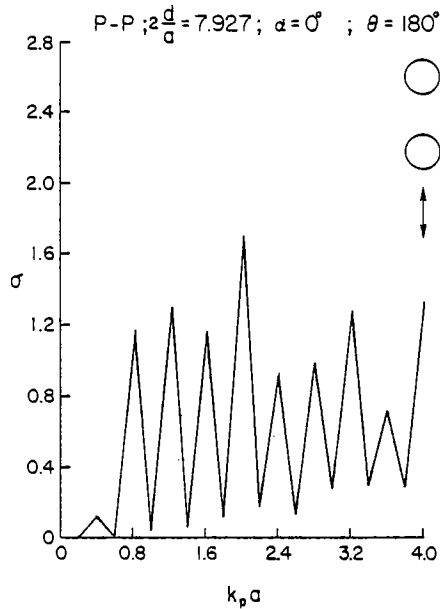


Fig. 6 Back scattering cross section as a function of frequency of identical spheres for incident P-waves.

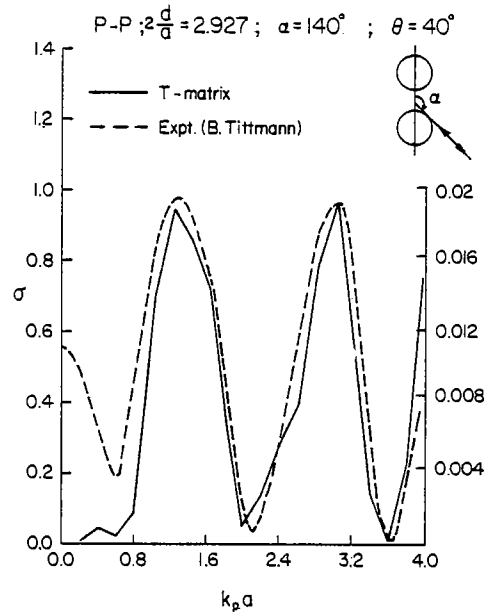


Fig. 7 Back scattering from two identical spheres, comparison of experiment and theory.

In Eq. (6), $k_\tau = k_p$ or k_s depending on the row index of the appropriate T-matrix element. This expression for the T-matrix is quite well suited for '2d' large. The disadvantage is that it is no longer independent of the scattering geometry. The major computation in Eq. (6) can however be performed independent of scattering geometry.

If the matrix inverses appearing in Eq. (3)

are expanded, one can identify the various multiple scattering processes that contribute to the total scattered field. If one wants to include only single scattering, then

$$T(1,2) \rightarrow R(\vec{d})T^1R(-\vec{d}) + R(-\vec{d})T^2R(\vec{d}) \quad (7)$$

The amplitude of the scattered longitudinal field at distances far from the origin is given by

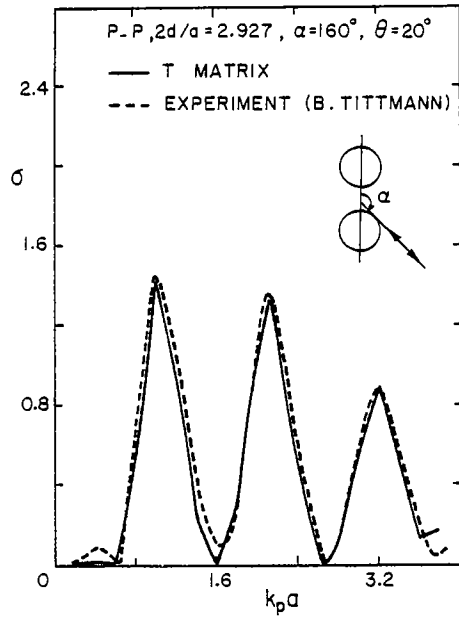


Fig. 8 Back scattering from two identical spheres, comparison of experiment and theory.

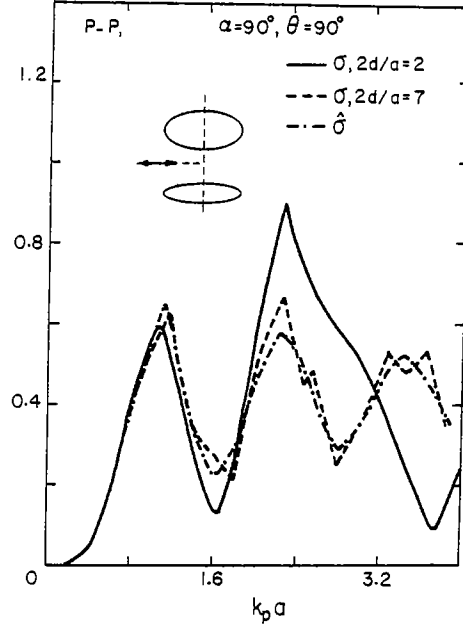


Fig. 9 Back scattering cross section of two spheroids, $b_1/a = 0.5$ and $b_2/a = 0.33$, for incident P-waves.

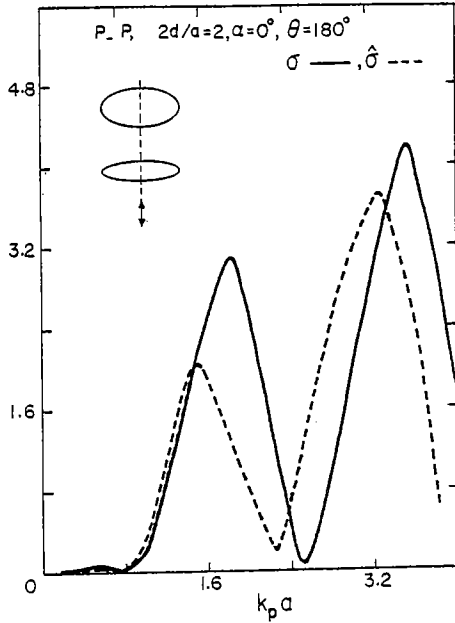


Fig. 10 Back scattering cross section of two spheroids, $b_1/a = 0.5$ and $b_2/a = 0.33$, for incident P-waves.

$$f(\theta, \phi) = \sqrt{\frac{c_s}{c_p}} \sum_{n=0}^{\infty} \sum_{m=0}^n \epsilon_{nm} i^{-n} p_n^m(\cos \theta) \times \{f_{1nm1} \cos m\phi + f_{1nm2} \sin m\phi\}. \quad (8)$$

The scattered energy or the cross section is given by

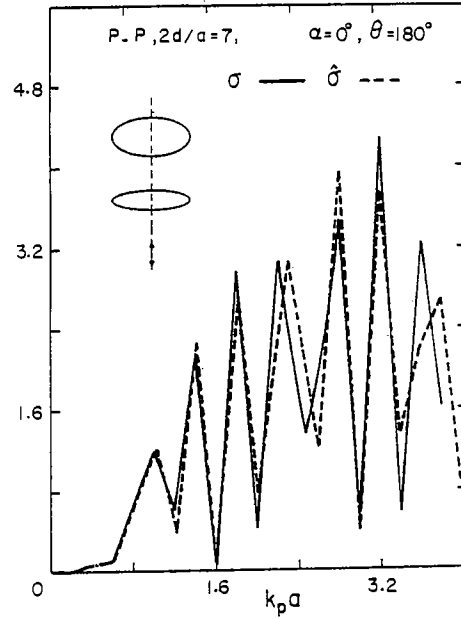


Fig. 11 Back scattering cross section of two spheroids, $b_1/a = 0.5$ and $b_2/a = 0.33$, for incident P-waves.

$$\sigma(\theta, \phi) = |f(\theta, \phi)|^2 / (k_p a)^2 \quad (9)$$

where 'a' is a characteristic dimension of the scatterer. Equations (8) and (9) may be used for both single and multiple scatterer configurations.

In the numerical results that follow, if the single scattering approximation is used for $T(1,2)$ (Eq. 7), the scattering cross section is

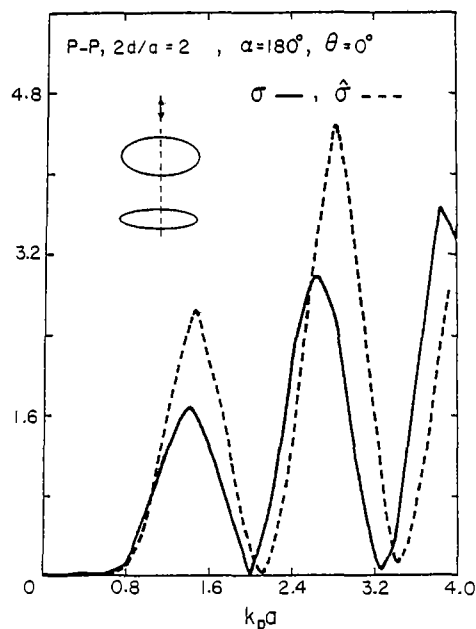


Fig. 12 Back scattering cross section of two spheroids, $b_1/a = 0.5$ and $b_2/a = 0.33$, for incident P-waves.

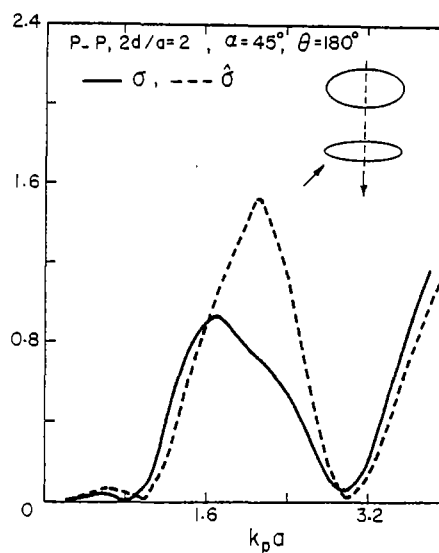


Fig. 14 Bistatic cross section of two spheroids, $b_1/a = 0.5$ and $b_2/a = 0.33$ for incident P-waves.

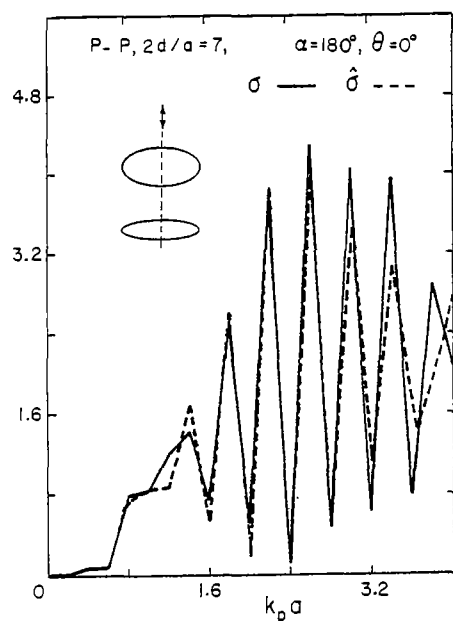


Fig. 13 Back scattering cross section of two spheroids, $b_1/a = 0.5$ and $b_2/a = 0.33$, for incident P-waves.

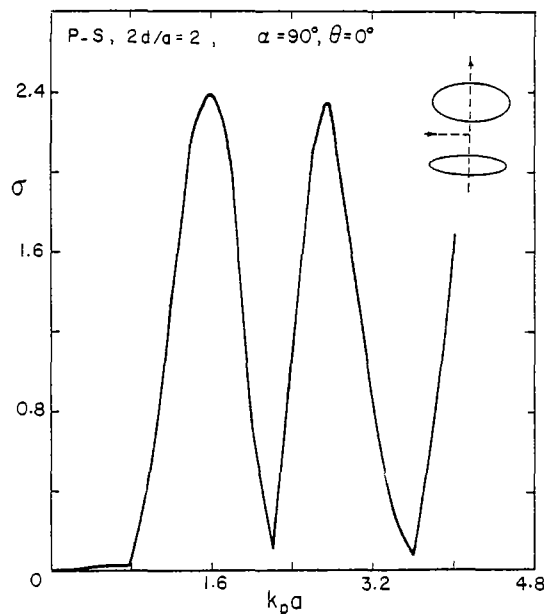


Fig. 15 Mode converted bistatic cross section (P to S) of two spheroids, $b_1/a = 0.5$ and $b_2/a = 0.33$.

distinguished as $\hat{\sigma}$. The two forms σ and $\hat{\sigma}$ are compared for several two scatterer configurations. It must be noted that although $\hat{\sigma}$ may be called a single scattering approximation, it still depends on the distance between the scatterers since the two single scattered complex amplitudes are added together with the proper phase. In the strict sense, a single scattering approximation would just correspond to adding the cross sections of the individual scatterers and all knowledge of the relative phase would be lost. This result is

completely independent of the distance between the scatterers and is distinguished as $\sigma_{S,S}$. We also observe that for back scattering at 90° incidence for example, the two single scattered amplitudes are in phase and $\hat{\sigma} = 2\sigma_{S,S}$.

In Fig. 4, the back scattering cross section is plotted as a function of $k_p a$ for P-wave incidence perpendicular to the line joining two identical spheres of radius a . In this case $\hat{\sigma} = 2\sigma_{S,S}$ as discussed above. It is seen that σ approaches $\hat{\sigma}$

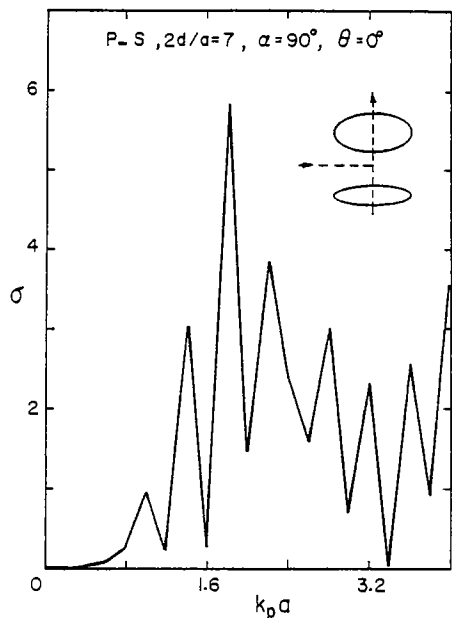


Fig. 16 Mode converted bistatic cross section (P to S) of two spheroids, $b_1/a = 0.5$ and $b_2/a = 0.33$.

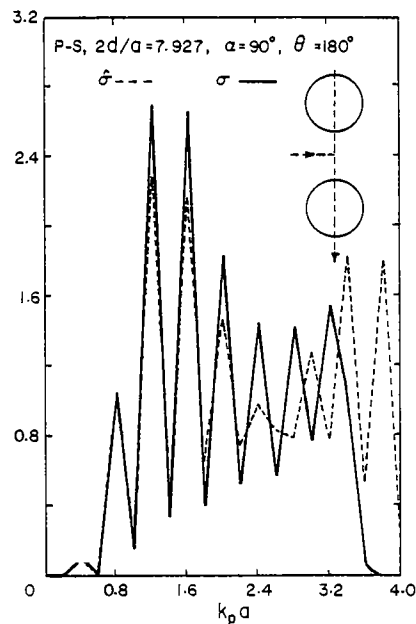


Fig. 18 Mode converted bistatic cross section of two identical spheres.

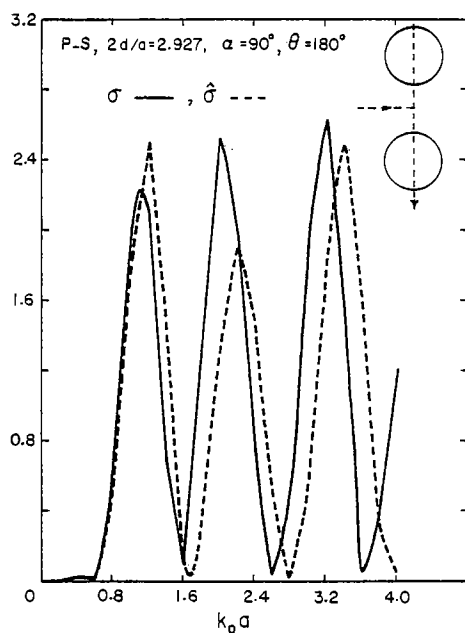


Fig. 17 Mode converted bistatic cross section of two identical spheres.

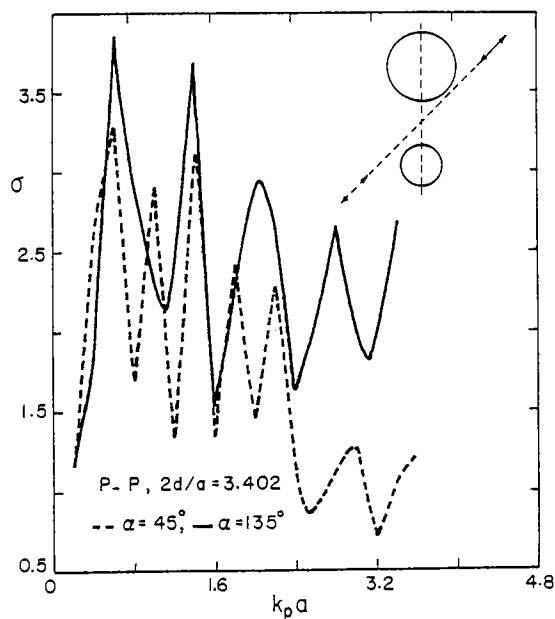


Fig. 19 Back scattering cross section for incident P-waves of two dissimilar spheres, ratio of radii = 3.0, 'a' is the radius of the small sphere.

as the distance between the two spheres increases. In Fig. 5, the back scattering cross section is plotted for P-waves incident along the line joining the two spheres. It is seen that even when the distance between the two spheres is as small as $2.927a$, σ and $\hat{\sigma}$ compare very well and display sharp zeroes. The spacings of the zeroes can be correlated to the interference of waves that creep around each of the spheres. The path difference between the two waves is twice the distance between the centers of the spheres and shows up in the

spacing of the minima. In Fig. 6 we have the same scattering geometry, but now the distance between the spheres has increased to $7.927a$, resulting in very closely spaced minima. In this case σ was almost equal to $\hat{\sigma}$ and hence $\hat{\sigma}$ is not displayed in the graph. In Figs. 7 and 8, for $\alpha = 140^\circ$ and $\alpha = 160^\circ$, the back scattering cross section is compared with experimental results showing excellent agreement. The results were plotted on the same graph by matching just one point, the maximum value of the cross section.

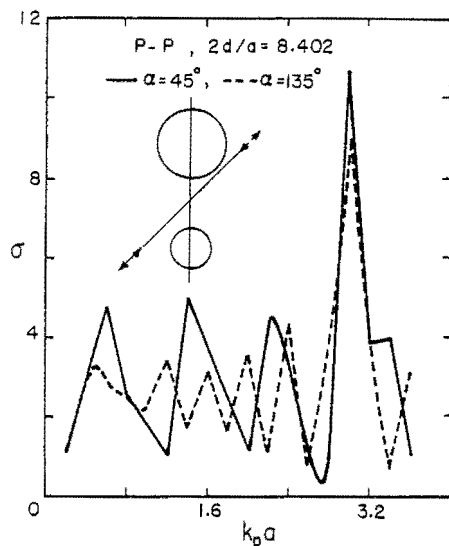


Fig. 20 Back scattering cross section for incident P-waves of two dissimilar spheres, ratio of radii = 3.0, 'a' is the radius of the small sphere.

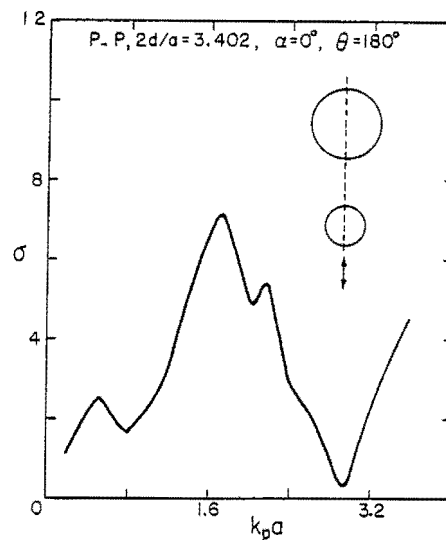


Fig. 22 Back scattering cross section for incident P-waves of two dissimilar spheres, ratio of radii = 3.0, 'a' is the radius of the small sphere.

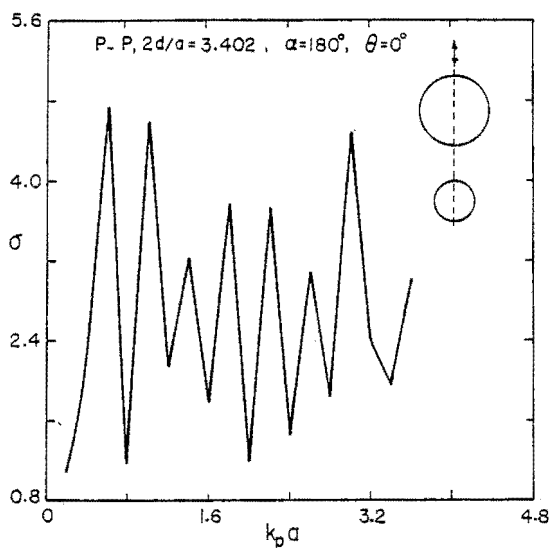


Fig. 21 Back scattering cross section for incident P-waves of two dissimilar spheres, ratio of radii = 3.0, 'a' is the radius of the small sphere.

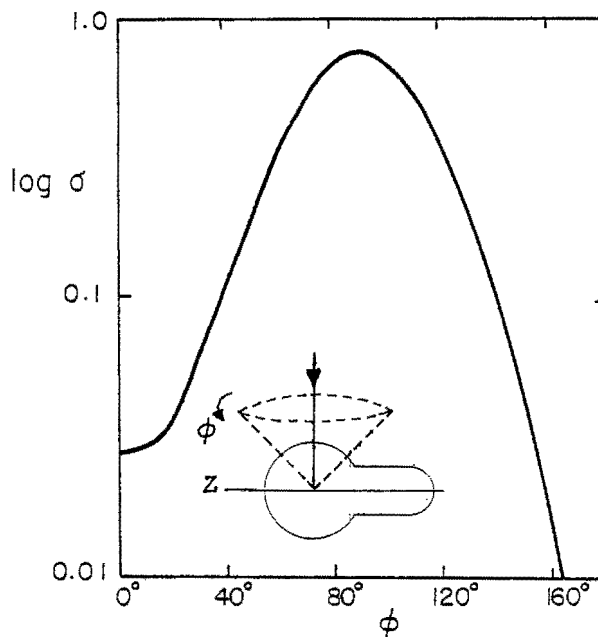


Fig. 23 Angular variation of the bistatic cross section of 'Pinnocchio' (Fig. 26) for P-waves incident broadside at $k_p a = 2.0$.

In Figs. 9-14, the back scattering cross section of two dissimilar oblate spheroids, shown in Fig. 1a is considered. The minor to major axis ratios were taken to be 0.5 and 0.33. Although interference of creeping waves does show up in the cross section, specularly reflected waves also contribute to the interference pattern, unlike the case of two identical spheres. In Fig. 15-18, the mode converted cross section is displayed for the geometries in Fig. 1a and 1b.

The next geometry that is considered is the

case of two dissimilar spheres of radii a_2 and a_1 , with $a_2/a_1 = 2.976$ (see Fig. 1c). In Fig. 19, the back scattering cross section for $\alpha = 45^\circ$ is compared with that for $\alpha = 135^\circ$ when the distance between centers is $3.4a_1$. In Fig. 20, the distance has increased to $8.4a_1$, and cross sections for $\alpha = 45^\circ$ and $\alpha = 135^\circ$ are again compared. It is also interesting to compare Fig. 19 with Figs. 21 and 22. Figure 21 is the back scattering cross section for $\alpha = 180^\circ$, illuminating the big sphere and Fig. 22 is the corresponding result for $\alpha = 0^\circ$ where the

small sphere is illuminated and also a large part of the big sphere. The results for the two cases are strikingly different. In fact, Fig. 21 looks almost like the scattering cross section of the big sphere of radius a_2 , if the abscissa is rescaled in terms of $k_p a_2$. The interference pattern is due to the path difference between the specularly reflected wave and a creeping wave.

Samples exist at the Rockwell Science Center for the geometries shown in Figs. 1a and 1c, however experimental results are available only for the case of identical spheres (Fig. 1a).

SCATTERING FROM COMPOUND FLAWS

The compound or odd shaped flaws that have been considered are shown in Figs. 2a and 2b. These are popularly known as "Micky Mouse" and "Pinnochio" respectively. Experimental data is available for both. To date most of the analytical-computational procedures have been confined to idealized scatterers like spheroids, penny shaped cracks or elliptical cracks. All these flaw surfaces can be described by a single equation. The geometries illustrated in Fig. 2 are however compound voids and different equations are needed to describe different portions of the surface. Hence these shapes are quite challenging for numerical computations.

Consider the geometry in Fig. 2a. At the junction, where the two spherical parts intersect, there is a discontinuity in the outward normal. Matrix methods are numerically unstable in the presence of such sharp concavities. Moreover the nature of the stress singularity at a sharp fracture such as this is unknown and remains one of the unsolved static boundary value problems in mechanics. Experimental evidence indicates that these stress singularities do not influence the scattered far field to any great extent. This has also been verified numerically for the two dimensional anti-plane problem. In this case the analytical form of the stress singularity is known.

Two different approaches were used. In one method, the small portion where the two spheres intersect was smoothed out by a straight line segment, in the second method Legendre polynomials were used to fit the contour smoothly. In the latter case there was a still a concavity, but it was not sharp. A third method of calculation is still in progress. This is to consider the void as a compound void with the two parts of the sphere just touching each other, the centers of the parts being separated by a finite distance. The T-matrix of each separate part is computed by closing off the open end by a straight line segment, on which the normal displacement must be prescribed. But the displacement on the straight line segment for the lower sphere will exactly cancel this when the two T-matrices are superposed in Eq. (3) to get the combined T-matrix. Preliminary results indicate that this approach is numerically much more stable and will enable us to consider much higher incident wave frequencies.

In Figs. 23-24, the angular behaviour of the scattering cross section for P-waves which are incident broad side on both samples. The actual scattering geometry is shown in the figures. In Fig. 24, the scattering cross section of a prolate spheroid and a sphere of the same over all

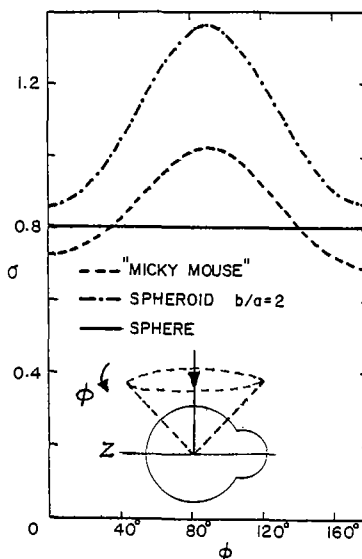


Fig. 24 Angular variation of the bistatic cross section compared for 'Micky Mouse' (Fig. 2a), prolate spheroid and sphere.

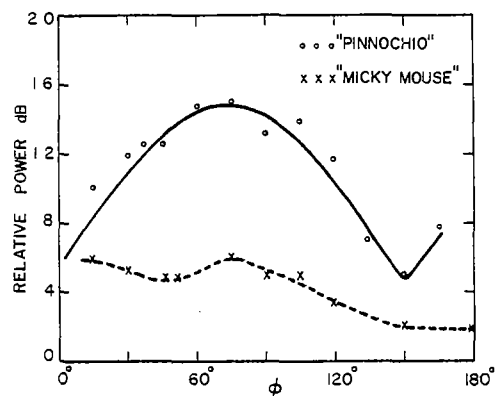


Fig. 25 Experimental results by B. Tittmann corresponding to calculations in Figs. 23 and 24.

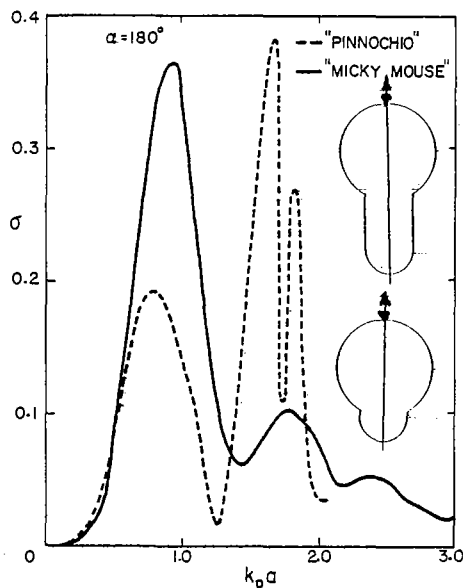


Fig. 26 Back scattering cross section for head on incidence of P-waves.

dimensions as "Micky Mouse" are displayed for purposes of comparison. Both figures indicate a sharp drop in the cross section at $\phi = 0^\circ$ and $\phi = 180^\circ$ corresponding to weak scattering from the two edges. For the case of "Pinnocchio", experimental results obtained by B. Tittmann shown on Fig. 25 seems to be in qualitative agreement. Comparison of the numerical results for the spectra with experiments is still in progress, since these became available only recently. In Figs. 26 and 27, the back scattering cross section as a function of frequency is displayed for incidence along the symmetry axes.

DYNAMIC STRESS CONCENTRATIONS

A method is presented for the calculation of dynamic stress concentration factors when a time harmonic SH-wave is incident upon a cylindrical cavity of arbitrary cross section. The stresses in the vicinity of the cavity are markedly different from those that would be present if the cavity were not present. This effect is known as dynamic stress concentration. The study for more general polarizations (in-plane problems) is still in progress. Exact determination of the dynamic stress concentration caused by a cylindrical cavity is only possible for a restricted class of cross sectional shapes, namely those for which the elastic wave differential operator is separable. Pao and Mow⁶ give a detailed description of the separation of variables approach for this problem. For more general cross sections, in particular if singular corners are present, a numerical technique is called for. We employ such a technique here.

Our algorithm is based on a method that has been called the null field method by Bates and Wall⁷ or the transition matrix (T-matrix) method. It reduces to the solution of a particular integral equation. This method has two major advantages over other methods when applied to the problems discussed here. The solution is unique and solutions of the complementary problem are decoupled. For cavities, the unknown function is the surface displacement. The evaluation of surface fields is much more difficult than the evaluation of scattered fields. In a sense, with the regular T-matrix approach used in the previous sections, the surface field is in fact calculated. But in the final analysis, due to the particular structure of the formulation (the use of the null field equation), the result is insensitive to an inaccurate determination of the surface field. For the problem at hand since the determination of the surface field is the end result, basis functions used to represent it must be picked with particular care.

When the scatterer has corners it is necessary to ensure that the basis used has the correct edge behaviour. Wedge functions are used for this purpose and they are found from the solution of the canonical problem of scattering from an infinite wedge. The surface of the cavity is divided into several regions and within each region an appropriate basis is used. The null field equations together with the constraint equations necessary to ensure continuity at the nodes are sufficient to solve for the unknown coefficients of the basis. If there are no corners, but just an increase in the stress concentration factor, an appropriate metric function is incorporated into basis representation. Details of the numerical procedure and more extensive results may be found in Ref. 4.

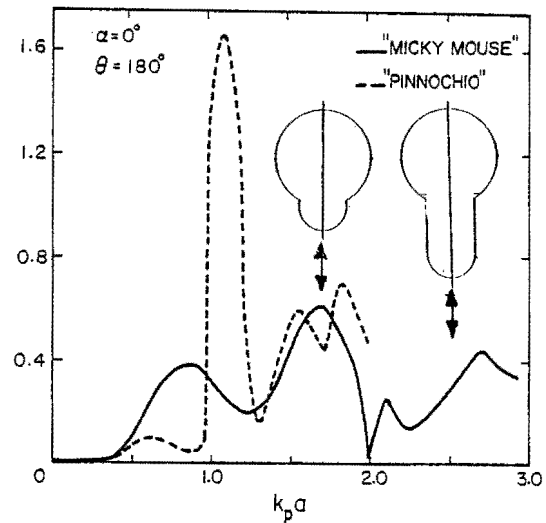


Fig. 27 Back scattering cross section for nose on incidence of P-waves.

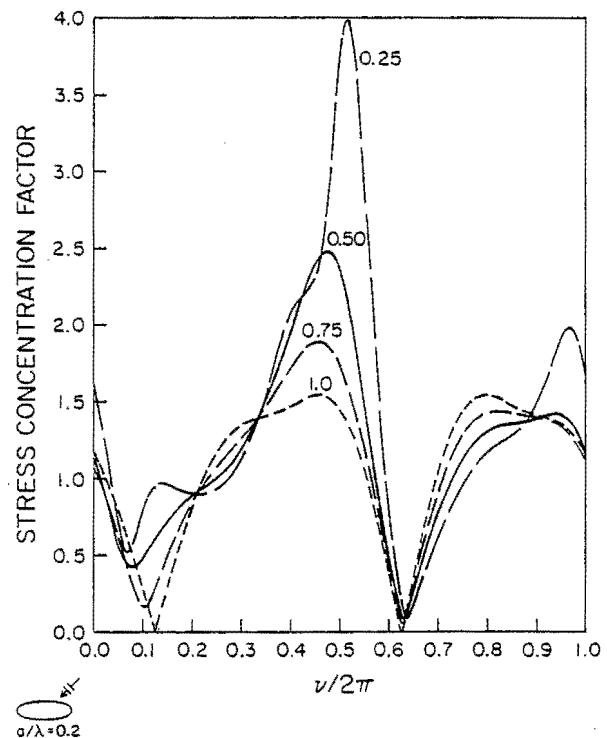


Fig. 28 Dynamic stress concentration on the surface of an elliptical cavity for four different minor to major axis ratios and incident SH-waves.

For the anti-plane problem, the boundary condition at the surface of the cavity may be stated as the vanishing of the normal traction

$$\sigma_{nz} = 0 \text{ on } S$$

where S is the surface of the cavity and \hat{n} is the outward normal in the x - y plane, the z -axis being parallel to the cylinder axis. The only non-zero stress component at the surface is then σ_{tz} where t is taken to be tangent to S in the x - y plane. In Figs. 28 and 29 σ_{nz} is plotted at all points on the boundary. In the abscissa $\phi/2\pi$ is the angular measure as one traverses the contour and it varies from 0 to 1 for a complete revolution. Figure 28 is for an elliptical cavity, the scattering geometry being displayed in the lower left corner. If 'a' is the semimajor axes of the ellipse and ' λ ' the incident wavelength a/λ is taken to be 0.2 corresponding to $ka = 1.4$. Four different minor to major axis ratios ranging from 0.25 to 1.0 are considered for this frequency. In Fig. 29, a cavity with corners arising from the sharp intersection of two circles is considered. In this case for 45° incidence, the stress concentration σ_{tz} is plotted for three values of the a/λ ratio 0.02, 0.2 and 0.4.

We conclude this section by observing that the success of this method depends on a good knowledge of the approximate behaviour of the stress in the vicinity of the scatterer. For three dimensional scatterers, many of the canonical problems are unsolved. The choice of appropriate basis functions at corners is crucial. The sharp singularities in the stress manifest themselves as barely discernible discontinuities in plots of the surface displacement, so that the latter must be calculated very accurately.

MULTIPLE SCATTERING CONFIGURATIONS WITH NO ROTATIONAL SYMMETRY

All the cases considered above for both multiple and compound flaws possessed an axis of rotational symmetry. Since vector spherical functions were used to describe the fields, the rotational symmetry renders all matrices diagonal in the azimuthal index. This simplifies the calculation enormously. Without this symmetry matrix sizes will become so large even at small values of kpa 1.0 to make computations unfeasible. However, the need exists for long wavelength scattering information from non-axis symmetric configurations. It is for this particular application that we propose the following. The formalism that is given below is in principle applicable for the range of frequencies for which the T-matrix of the individual scatterer can be computed, the limitation is in the machine computations.

We consider two coordinate systems centered at 0, x - y - z and x' - y' - z' respectively. Let α , β , γ be the Euler angles of the primed system with respect to the unprimed system (Fig. 30). It is often desirable to calculate the T-matrix of an individual scatterer with respect to a coordinate system that is chosen based on the geometrical symmetries of the scatterer. This will minimize computations. If the scatterer has an axis of rotational symmetry, the T-matrix is diagonal in the azimuthal index. However, it may be necessary to express this T-matrix in a different coordinate system, say the

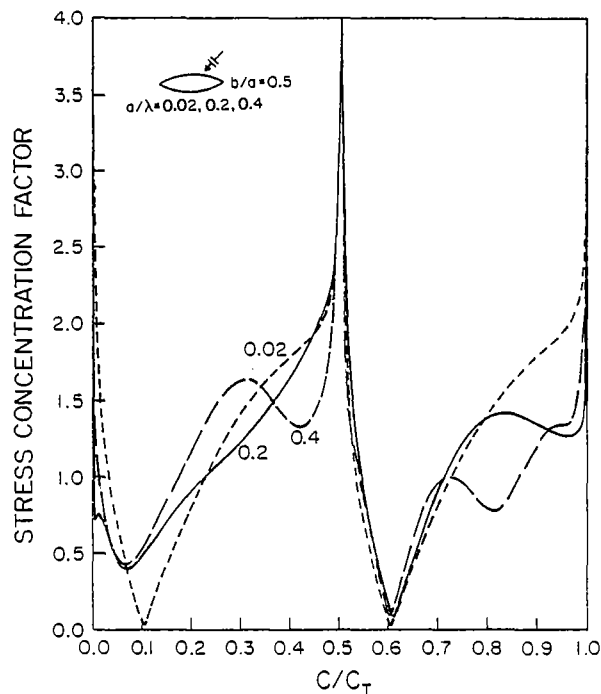


Fig. 29 Dynamic stress concentration on the surface of a cylindrical lens shaped cavity with sharp corners for different incident SH-wave frequencies, c/c_T is the normalized contour length.

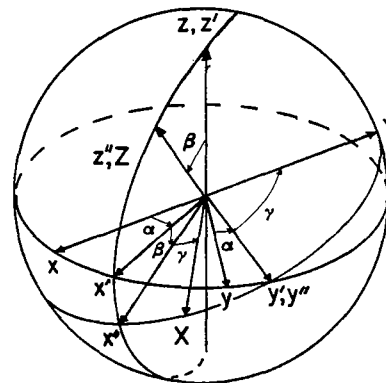


Fig. 30 Euler angles for rotation of coordinate systems.

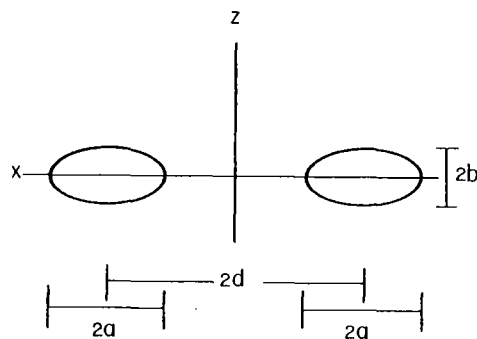


Fig. 31 Spheroidal scatterers with no rotational axis of symmetry.

primed system because the experimental set up may necessitate it or there may be another scatterer with its axis of symmetry aligned with the primed system. For the particular application we have in mind, refer to Fig. 31. Two spheroidal scatterers are considered with their centers separated by a distance '2d', perpendicular to the axis of rotational symmetry. In the previous sections the translation was along the axis of symmetry. The resulting configuration is not rotationally symmetric, hence the total T-matrix loses its block diagonal property. In this case also the expression for $T(1,2)$ given in Eqs. 3 or 6 is applicable if one keeps the general form of the translation matrices. However, it is more convenient to express the T-matrix of the individual spheroids in coordinate system that is rotated by a 90° angle and then perform the translation along this new z-axis.

The transformation of the T-matrix under an Euler rotation may be conveniently expressed by noting that the spherical harmonics used in deriving the T-matrix are the eigenfunctions of the rotation operator^{5,8}. Thus if T' is the T-matrix in the primed system, then it is related to the T-matrix of the unprimed system according to

$$T' = D^{-1}(\alpha, \beta, \gamma) T D(\alpha, \beta, \gamma) \quad (10)$$

where the rotation matrix D is given by

$$D_{m'm}^n(\alpha, \beta, \gamma) = e^{im'\alpha} d_{mm'}^n(\beta) e^{im\gamma} \quad (11)$$

where

$$d_{mm'}^n(\beta) = \left[\frac{(n+m')!(n-m)!}{(n+m)!n!} \right]^{\frac{1}{2}} \left(\cos \frac{\beta}{2} \right)^{m'+m} \times \left(\sin \frac{\beta}{2} \right)^{m'-m} P_{n-m'}^{(m'-m, m'+m)}(\cos \beta) \quad (12)$$

In Eq. (12), P_n^j are the Jacobi polynomials which can be expressed in terms of the associated Legendre polynomials. For more details on Eqs. (11) and (12) we refer the reader to Edmonds⁹. If T^1 and T^2 in Eqs. (3) and (6) are replaced by $D^{-1}T^1D$ and $D^{-1}T^2D$, we obtain $T(1,2)$ for the configuration shown in Fig. 31. Numerical computations at wavelengths long comparable to the overall dimensions of the configuration are still in progress.

ACKNOWLEDGEMENTS

This research was supported by the Center for Advanced NDE, operated by the Science Center, Rockwell International for DARPA/AFML under contract #F33615-80-C-5004. The help of Dr. Bo Peterson in some phases of the computation is gratefully acknowledged.

REFERENCES

1. V.V. Varadan and V.K. Varadan, 'Elastic wave scattering by rough flaws and cracks', Interdisciplinary Program for Quantitative Flaw Definition, Special Report fifth year effort, prepared for ARPA/AF by B. Thompson, Center for Advanced NDE, Rockwell International, Thousand Oaks, California 91360 (1979).
2. B. Peterson and S. Ström, 'T-Matrix for electromagnetic scattering from an arbitrary number of scatterers and representations of $E(3)$ ', Phys. Rev. D, 8, 3661 (1973).
3. A. Boström, 'Multiple scattering of elastic waves by bounded obstacles', J. Acoust. Soc. Am. 67, 399 (1980).
4. D.J.N. Wall, V.V. Varadan and V.K. Varadan, 'Dynamic stress concentrations of cylindrical cavities with sharp and smooth boundaries I. SH waves', Report submitted to Center for Advanced NDE, Rockwell International (1980), Also submitted for publication.
5. V.V. Varadan, 'Elastic wave scattering', in Acoustic, Electromagnetic and Elastic Wave Scattering - Focus on the T-Matrix Approach edited by V.K. Varadan and V.V. Varadan, Pergamon Press, New York (1980).
6. Y.H. Pao and C.C. Mow, 'Diffraction of elastic waves and dynamic stress concentrations', Crane Russak, New York (1973).
7. R.H.T. Bates and D.J.N. Wall, 'Null field approach to scalar diffraction I. General Method', Phil. Trans. R. Soc. Lond. A287, 45 (1977).
8. V.V. Varadan and V.K. Varadan, 'Multiple scattering of electromagnetic waves by randomly distributed and oriented scatterers', Phys. Rev. D, 19, 2480 (1980).
9. A.R. Edmonds, 'Angular momentum in quantum mechanics', Princeton University Press, Princeton, New Jersey (1957).